

## Full Length Article

Influence of the molten SrCl<sub>2</sub> treatment on the surface structure and photochemical reactivities of SrTiO<sub>3</sub>Mingyi Zhang<sup>a</sup>, Zhitao Guo<sup>b</sup>, Andrew J. Gellman<sup>b</sup>, Paul A. Salvador<sup>a</sup>, Gregory S. Rohrer<sup>a,\*</sup><sup>a</sup> Department of Materials Science and Engineering, Carnegie Mellon University, Pittsburgh, PA 15213, USA<sup>b</sup> Department of Chemical Engineering, and Wilton E. Scott Institute for Energy Innovation, Carnegie Mellon University, Pittsburgh, PA 15213, USA

## ARTICLE INFO

## Keywords:

Molten salt treatment  
 Photocatalytic hydrogen generation  
 SrTiO<sub>3</sub> photocatalysts  
 Charge separation  
 Atomic force microscopy

## ABSTRACT

Al-doped SrTiO<sub>3</sub> synthesized in a SrCl<sub>2</sub> melt is among the most efficient known photocatalysts for water splitting. Although the effect of Al<sup>3+</sup> incorporation has been widely discussed, the role of the molten SrCl<sub>2</sub> remains unclear. Herein, we report the influence of the molten SrCl<sub>2</sub> treatment and a comparable molten KCl treatment on the surface structure and composition of SrTiO<sub>3</sub> using AFM and XPS. The hydrogen evolution rates of particulate Al-doped SrTiO<sub>3</sub> photocatalysts were measured with a parallelized and automated photochemical reactor. In SrCl<sub>2</sub>, it is found that 3% to 5% of the SrTiO<sub>3</sub> dissolves in the melt, revealing a new hydroxyl-rich surface. The melt reacts with the alumina crucible to form Sr<sub>3</sub>Al<sub>2</sub>O<sub>6</sub>, ultimately leading to the elimination of the melt. In addition, the surface potential difference between (100) and (110) surfaces increases from 0.07 V to 0.21 V after the treatment, allowing for enhanced separation of photogenerated charge carriers and leading to improved photocatalytic reactivity. When heated in KCl, the SrTiO<sub>3</sub> surfaces reconstruct and this changes the spatial distribution of photocathodic and photoanodic reaction sites.

## 1. Introduction

Photocatalytic water splitting on a semiconductor surface is a promising method for converting solar energy into hydrogen fuel [1-3]. Over the past decades, a great number of semiconductors have been reported to be capable of splitting water. Among them, molten SrCl<sub>2</sub> synthesized Al-doped SrTiO<sub>3</sub> is one of the most efficient water splitting photocatalysts. In 2013, Kato et al. heated SrTiO<sub>3</sub> powders prepared with a polymerized complex method in different molten salts, such as NaCl, KCl, LiCl, and SrCl<sub>2</sub> [4]. All of the salts changed the particle morphology, but the treatment in KCl improved the reactivity. Later, Domen and coworkers altered the ratio of SrCl<sub>2</sub> to SrTiO<sub>3</sub> and found that the photocatalytic reactivity of SrTiO<sub>3</sub> could be significantly improved by heating it in an excess amount of molten SrCl<sub>2</sub>; this was attributed mainly to the dissolution of a small amount of Al into the SrTiO<sub>3</sub> from the Al<sub>2</sub>O<sub>3</sub> crucibles [5,6]. Since then, several methods have been reported to improve the performance of this material, such as loading anodic cocatalysts [7,8], manipulating particle shape and size [9], and photodepositing cocatalysts on different facets [10]. It is understood that Al<sup>3+</sup> can reduce the formation of the Ti<sup>3+</sup> deep recombination sites and increase the charge carriers' lifetime, and this has been confirmed

by Zhao et al. using XPS and DFT methods [11]. More recently, research has shown that the reactivity can be further improved by co-doping SrTiO<sub>3</sub> with both Al<sup>3+</sup> and Zr<sup>4+</sup>, Ta<sup>5+</sup>, or La<sup>3+</sup> [12-14].

While Al doping has been confirmed to be beneficial to the photocatalytic reactivity of SrTiO<sub>3</sub>, the role of the molten SrCl<sub>2</sub> treatment remains unclear. This simple treatment involves heating SrTiO<sub>3</sub> in an excess amount of SrCl<sub>2</sub> at a temperature between the melting point and boiling point of SrCl<sub>2</sub> in an alumina crucible and produces a highly reactive SrTiO<sub>3</sub> photocatalyst. It is noted that all the studies described previously have employed this molten SrCl<sub>2</sub> treatment (also referred to as the SrCl<sub>2</sub> flux treatment) for doping. Previous studies show that Al-doped SrTiO<sub>3</sub> synthesized via a solid state method [6] or a hydrothermal method [15] are less reactive than those prepared by the molten salt method, implying the importance of the molten SrCl<sub>2</sub> treatment. Ham et al. [6] proposed that part of the SrTiO<sub>3</sub> particles dissolve and recrystallize in the presence of the SrCl<sub>2</sub> melt so that the crystallinity is improved. Motivated by these results, we desire to understand how the molten SrCl<sub>2</sub> treatment influences the chemical composition and structure of the SrTiO<sub>3</sub> surface.

Because it is difficult to characterize the surfaces of the small particles typically used as catalysts, we also perform the same molten SrCl<sub>2</sub>

\* Corresponding author.

E-mail address: [gr20@andrew.cmu.edu](mailto:gr20@andrew.cmu.edu) (G.S. Rohrer).<https://doi.org/10.1016/j.apsusc.2023.158111>

Received 13 June 2023; Received in revised form 14 July 2023; Accepted 25 July 2023

Available online 26 July 2023

0169-4332/© 2023 The Author(s). Published by Elsevier B.V. This is an open access article under the CC BY license (<http://creativecommons.org/licenses/by/4.0/>).

treatment on SrTiO<sub>3</sub> single crystal substrates of known orientations and investigate how it influences the photochemical reactivities. Air annealed substrates and molten KCl treated substrates have been prepared and employed for comparisons. The surface potentials were measured by Kelvin probe force microscopy (KFM) and correlated to the relative reactivities measured by photochemical marker reactions and atomic force microscopy (AFM). Comparing these results to X-ray photoelectron spectra (XPS) of the same surfaces, we found that the concentration of surface –OH groups, the surface potential, and the photochemical properties are all correlated. The molten SrCl<sub>2</sub> treatment significantly enriches the concentration of surface –OH groups and decreases the surface potential. Meanwhile, the surface potential difference between the (100) and (110) surfaces increases from 0.07 V to 0.21 V after the molten SrCl<sub>2</sub> treatment, allowing for enhanced charge separation between the two surfaces and leading to improved photocatalytic reactivity for hydrogen production by treated SrTiO<sub>3</sub> powders.

## 2. Experimental methods

### 2.1. Sample preparation

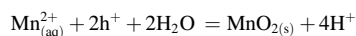
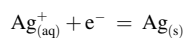
Chemical-mechanical polished (100) and (110) oriented SrTiO<sub>3</sub> single crystals (single side polished) were purchased from MSE Supplies with a size of 5 × 5 × 0.5 mm. The crystals were ultrasonically washed in methanol for 10 min and then annealed at 1100 °C in air for 6 h in a covered alumina crucible. After annealing, some crystals were treated in either a SrCl<sub>2</sub> melt or a KCl melt to study the effect of the molten salt treatment. In a typical treatment, the air annealed crystal was placed in a 20 ml covered alumina crucible (Sigma-Aldrich) with the polished side facing up, and then powders were placed on the top of the crystal with a molar ratio to SrTiO<sub>3</sub> of 10:1 for SrCl<sub>2</sub> (Alfa Aesar, 99.5 %) or 20:1 for KCl (Alfa Aesar, 99 %). The crucible was then transferred to a furnace and annealed at 1150 °C in air for 10 h. After annealing, the crystal was ultrasonically washed in DI water for 1 h and then washed in methanol and acetone each for 10 min.

Al-doped SrTiO<sub>3</sub> particulate catalysts were prepared using a hydrothermal approach reported by Dong et al. [16] In the synthesis, 0.2 ml of TiCl<sub>4</sub> (Sigma-Aldrich, 99 %) was dropped into a solution in an ice bath containing 25 ml of deionized water and 1 g of ethylene glycol surfactant (Alfa Aesar, 99+) with 1 mol % or 2 mol % of AlCl<sub>3</sub>·6H<sub>2</sub>O (Fisher Scientific) mixed with the precursors. After magnetic stirring for 5 min, 10 ml of SrCl<sub>2</sub> aqueous solution containing 0.42 g SrCl<sub>2</sub> (Sigma-Aldrich, 99.99 %) and 30 ml of LiOH aqueous solution containing 2.26 g LiOH (Sigma-Aldrich, 98 %) was added. After stirring for another 30 min, the resulting solution was transferred to a 100 ml Teflon-lined hydrothermal autoclave (Techinstro). The autoclave was then heated at 180 °C for 36 h in a furnace. After the thermal treatment, the solution was removed and the resulting precipitate was centrifuged four times at 4000 rpm for 12 min with deionized water and ethanol, respectively. Finally, the resulting precipitate was dried in an oven at 80 °C overnight. As for the SrCl<sub>2</sub> treatment, 0.3 g powder as prepared was mixed with SrCl<sub>2</sub> (Alfa Aesar, 99.5 %) in a ratio of 1:10 and annealed at 1150 °C in air for 10 h in an alumina crucible. The resulting mixture was centrifuged at 4000 rpm for 18 min, four times with deionized water and then four times with ethanol, and finally dried in an oven overnight. RhCrO<sub>x</sub> cocatalysts were loaded (0.1- wt% Rh and 0.1- wt% Cr) on all crystals using an impregnation method reported elsewhere [9,17].

### 2.2. Photochemical marker reaction

This method employs the photoreduction of Ag<sup>+</sup> or the photo-oxidation of Mn<sup>2+</sup> that leaves insoluble products on the surface at the sites of the reactions [18–20]. An O-ring was placed on the top of the single crystal sample and its interior volume was filled with 0.115 M AgNO<sub>3</sub> solution or 0.115 M MnSO<sub>4</sub> solution with unadjusted pH. A quartz coverslip was then placed on the top of the O-ring to seal the

solution without bubbles. The entire setup was then illuminated under a 150 W Xe lamp (Newport, Irvine, CA). For Ag<sup>+</sup> reduction, the sample was illuminated for 20 s for (110) crystals and 5 s for (100) crystals. For Mn<sup>2+</sup> oxidation, the sample was illuminated for 90 s for (110) crystals and 60 s for (100) crystals. Reaction conditions were adjusted so that the surface was only partially covered with the products owing to the fact that the (100) surface is much more reactive than the (110) surface [19,21], and the Mn<sup>2+</sup> oxidation is a relatively slow reaction compared with the Ag<sup>+</sup> reduction [22]. After illumination, the sample was rinsed in DI water and dried with a stream of argon. Before carrying out another experiment, the crystal surface was cleaned with cotton swabs and ultrasonically cleaned in acetone and methanol, respectively. The two reactions can be expressed in the following way:



Before and after the reaction, the surface topography was imaged by atomic force microscopy (AFM) with a Solver Next AFM (NT-MDT) or an NTEGRA AFM (NT-MDT) operated in semi-contact mode using a standard AFM probe (NCHR, NanoWorld). The local surface potential was measured by Kelvin Probe Force Microscopy (KFM) using a silicon AFM probe coated with Pt/Ir (NCHPT, NanoWorld). Before the measurement, the probes were calibrated using a Au (111) thin film sample. The Gwyddion software package was employed to analyze the data [23]. Photochemical reactivities are grouped into three categories by counting averaged deposits in a 1 μm<sup>2</sup> box region and presented in Table 1: High reactivity (>10 deposits), Mid reactivity (5–10 deposits), and Low reactivity (<5 deposits). Because different reaction conditions are used for different orientations, meaningful comparisons can only be made between specific orientations with different pre-treatments.

### 2.3. Photocatalytic water splitting experiment

The photocatalytic water splitting reaction was carried out using a high-throughput parallelized and automated photochemical reactor (PAPCR) [24]. The reactor employs a hydrogen sensitive film whose color changes from light to dark when exposed to hydrogen. The relationship between the local hydrogen concentration and film darkness has been calibrated and reported in detail in our previous work [9]. The image of the film was captured by a camera fixed on the top of the reactor. To measure the H<sub>2</sub> production rate, 10 mg of powder as prepared were placed into a glass vial with 0.4 ml of DI water whose pH was adjusted to pH 5, pH 7, pH 9, and pH 12 by adding nitric acid (Fisher Chemical) or NaOH (Fisher Scientific). The illumination was provided by two 100 W, 380 nm UV LEDs (Chanzone). The whole illumination lasted for 16 h, during which a total of 160 images were taken, with each image quantifying the hydrogen concentration within each vial.

## 3. Results

In a conventional molten salt process, the salt liquifies above the melting point and then solidifies on cooling. At the end of the process, the solid salt is the same phase as it was at the start of the process, but likely containing some impurities [25]. This is a good description of the

**Table 1**  
Photochemical reactivities and surface potential of the six SrTiO<sub>3</sub> single crystal surfaces.

Sample	Air annealed		SrCl <sub>2</sub> treated		KCl treated	
	cathodic	anodic	cathodic	anodic	cathodic	anodic
STO(100)	High 181 mV	High	Mid –62.9 mV	Low	Low 117 mV	High
STO(110)	Low 110 mV	Mid	High –271 mV	High	Low –32.3 mV	Low

molten KCl treatment (or other alkali metal chlorides). However, the  $\text{SrCl}_2$  process is not like this – at the process temperature, the salt reacts with both the  $\text{Al}_2\text{O}_3$  crucible and, to some extent, the  $\text{SrTiO}_3$ . By the end of the process, there is no (or very little)  $\text{SrCl}_2$  left in the crucible. When  $\text{SrCl}_2$  is melted in an alumina crucible (even without any  $\text{SrTiO}_3$  present), it wets and reacts with the crucible, forming yellow reaction products on the outer crucible sidewall. The resulting products were collected by centrifugation and characterized by XRD (see Fig. S1) and it was found that a large percentage of the salts have reacted with the crucible to form  $\text{Sr}_3\text{Al}_2\text{O}_6$  and then  $\text{Sr}_3\text{Al}_2(\text{OH})_{12}$  after rinsing in water. Based on the phase diagram of the  $\text{SrO-SrCl}_2$  system in Figure S2 [26],  $\text{SrO}$  is likely to form in the melt and react with  $\text{Al}_2\text{O}_3$ . Because of this, the actual time that the  $\text{SrTiO}_3$  is in contact with molten  $\text{SrCl}_2$  is much shorter than 10 h, as the melt composition changes, and the liquid disappears.

To eliminate the complication of the reaction with the alumina crucible, we also treated a  $\text{SrTiO}_3$  single crystal substrate in molten  $\text{SrCl}_2$  in a platinum crucible at  $1150^\circ\text{C}$  for 10 h. In contrast to what happened with the alumina crucible, the  $\text{SrCl}_2$  remained in the Pt crucible and, as shown in XRD (see Fig. S1 (b)), there was still  $\text{SrCl}_2$  at the end of the experiment. However, in this case, the crystal dissolved almost completely in the salt. Based on these observations, we reach the following conclusions. First, given sufficient time and excess salt,  $\text{SrTiO}_3$  will dissolve in molten  $\text{SrCl}_2$ . However, when  $\text{SrTiO}_3$  is heated in the presence of liquid  $\text{SrCl}_2$  in an alumina crucible, there is a side reaction with the crucible that depletes the molten salt after dissolving only a small amount of the  $\text{SrTiO}_3$ .

$\text{SrTiO}_3$  particles were prepared via a hydrothermal method [16] with a specific amount of  $\text{AlCl}_3$  added along with the precursors. SEM images of  $\text{SrTiO}_3$  particles with 1 % and 2 %  $\text{Al}^{3+}$  added are given in the first column of Fig. 1(a), denoted as Hydro1 % and Hydro2 %. It is assumed that Al atoms were uniformly distributed within these crystals. After loading  $\text{RhCrO}_x$  cocatalysts (0.1 wt% Rh and Cr), photocatalytic water splitting experiments have been carried out on Hydro1 % and Hydro2 % crystals. However, no  $\text{H}_2$  evolution was detected by the PAPCR either in pure water or an aqueous methanol solution. Next, Hydro1 % and Hydro2 % crystals were modified by the molten  $\text{SrCl}_2$  treatment in an

$\text{Al}_2\text{O}_3$  crucible. The resulting crystals are referred to as Hydro1 %-sA and Hydro2 %-sA shown in the second column of panel 1(a) and they have morphologies similar to Hydro1 % and Hydro2 %, but their sharp edges become rounded, consistent with our previous report [9]. Again, the  $\text{RhCrO}_x$  (0.1 wt% Rh and Cr) cocatalysts were loaded. These crystals had significantly enhanced reactivities compared to those crystals that have not been heated in the  $\text{SrCl}_2$  melt. As shown in Fig. 1 (b) and (c), the water splitting reactivities of these crystals reached  $6.5\mu\text{mol h}^{-1}$  in pure water. The corresponding surface area specific rates are shown in Figure S3. Note that we have even tried powders with much higher Al concentrations, but they still did not produce  $\text{H}_2$  in the absence of the molten  $\text{SrCl}_2$  treatment. The experiment above was inspired by the idea that Al-doping during the hydrothermal synthesis and during the  $\text{SrCl}_2$  treatment might lead to a different material. The results confirmed that the  $\text{SrCl}_2$  treatment is necessary to prepare highly reactive  $\text{SrTiO}_3$  photocatalysts. However, the particles are small, and it is difficult to directly characterize their surfaces before and after the  $\text{SrCl}_2$  treatment. Therefore, we reproduced this experiment by heating  $\text{SrTiO}_3$  single crystal substrates in the melt and compared their surface properties before and after the treatment.

The topographic AFM image of the surface of a  $\text{SrTiO}_3$  (1 1 0) single crystal annealed in air at  $1100^\circ\text{C}$  for 6 h is shown in Fig. 2(a). The surface is made up of large flat (1 1 0) terraces and long steps with near [1 0 0] orientations [19]. After the sample was immersed in a  $\text{AgNO}_3$  ( $\text{MnSO}_4$ ) solution and illuminated, new bright contrast appeared on the surface as shown in Fig. 2(b) and (c), corresponding to reduced metallic silver (Mn oxides). It is observed that the photochemical reaction is anisotropic; Ag reduction prefers to occur on the (1 0 0) edges and Mn oxidation mainly occurs on the (1 1 0) terraces, which is consistent with previous reports [19,21].

Two additional air-annealed  $\text{SrTiO}_3$  (1 1 0) single crystals were treated in molten  $\text{SrCl}_2$  and KCl, and the topographic AFM images of their surfaces are presented in Fig. 3 (a) and (d), respectively. The surface restructures in both treatments. For the sample treated in the  $\text{SrCl}_2$  melt, the large terraces were replaced by very fine terraces as large as a few tens of nanometers with long curved edges. At the same time, it seems that dislocations were etched in the melt as multiple etch pits are

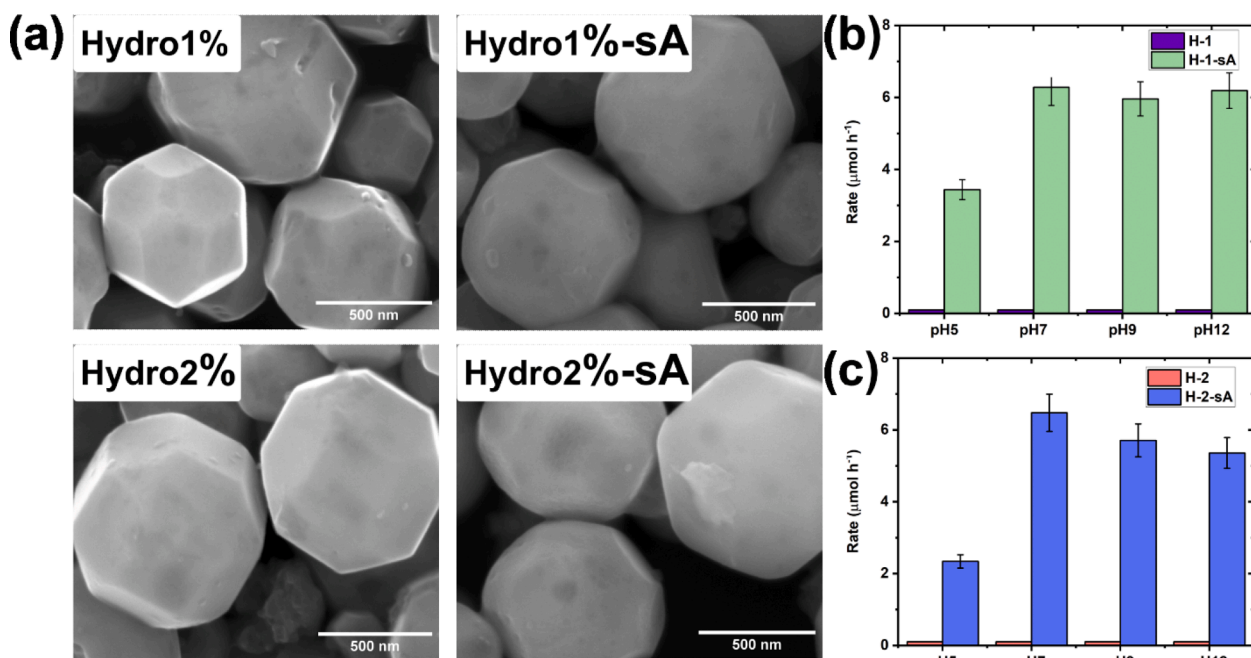
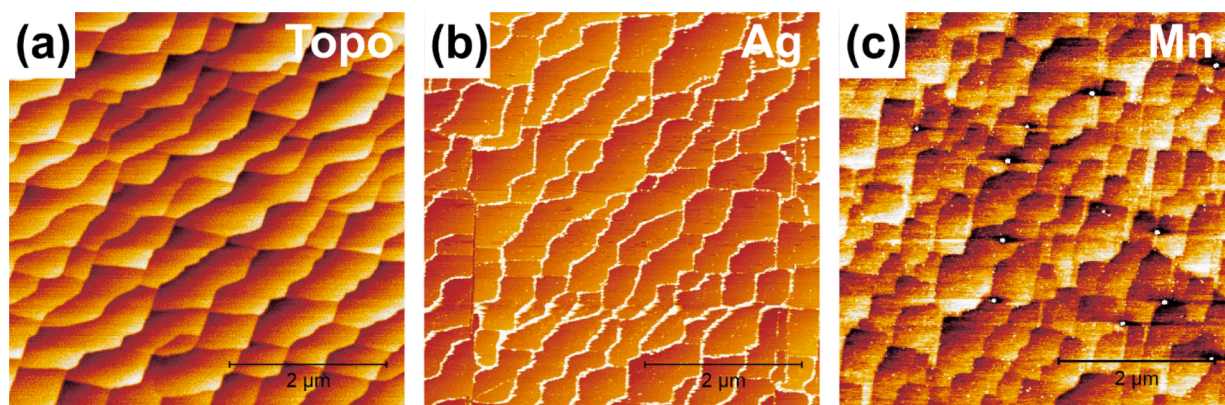
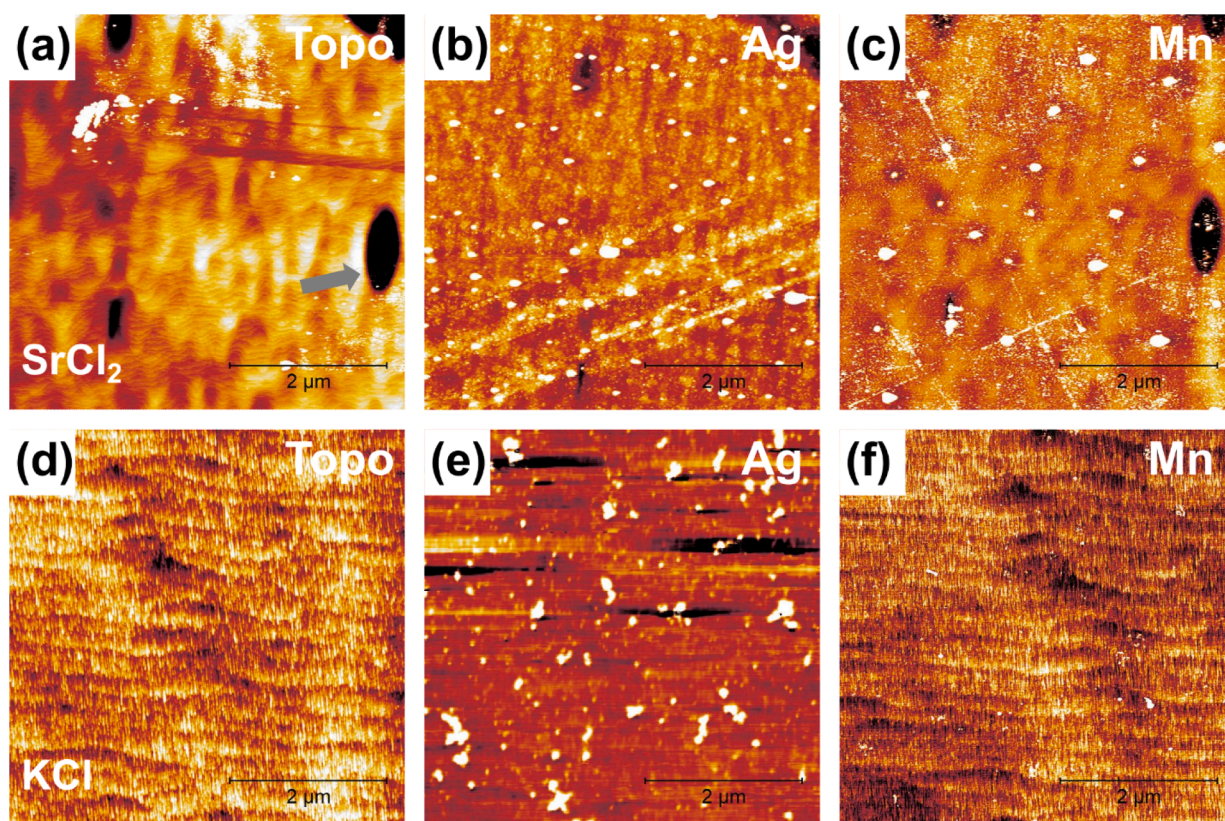


Fig. 1. (a) SEM images of Hydro1 % and Hydro2 % crystals and the resulting crystals after modifying by molten  $\text{SrCl}_2$  in an alumina crucible. The scale bar represents 500 nm. (b) and (c) show rates ( $\mu\text{mol h}^{-1}$ ) of  $\text{H}_2$  generation by Hydro1 % and Hydro2 % crystals before and after the  $\text{SrCl}_2$  treatment, respectively. The bars represent the standard deviations. Surface area specific rates are shown in Fig. S3.



**Fig. 2.** Topographic AFM image of an air annealed SrTiO<sub>3</sub> (110) surface is given in (a). Images of the surface after photoreduction of Ag<sup>+</sup> and photooxidation of Mn<sup>2+</sup> are shown in (b) and (c). The dark-to-light vertical contrast is (a): 0–3 nm, (b): 0–10 nm, (c): 0–4 nm.



**Fig. 3.** Topographic AFM images of air annealed SrTiO<sub>3</sub> (110) single crystal surfaces after treating in molten (a) SrCl<sub>2</sub> and (d) KCl. Panel (b) and (c) show AFM images of the SrCl<sub>2</sub> treated (110) surface after Ag<sup>+</sup> photoreduction and Mn<sup>2+</sup> photo-oxidation. Panel (e) and (f) show AFM images of the KCl treated (110) surface after Ag<sup>+</sup> photoreduction and Mn<sup>2+</sup> photo-oxidation. The dark-to-light vertical contrast is (a): 0–4 nm, (b): 0–15 nm, (c): 0–5 nm, (d): 0–3 nm, (e): 0–8 nm, (f): 0–3 nm. An etch pit has been labeled with an arrow in (a).

observed on the surface (one is marked with an arrow). We measured the mass of the sample before and after the molten SrCl<sub>2</sub> treatment and found that the mass was reduced from 0.0653 g to 0.0630 g (~3.5 % loss), indicating that some of the crystal dissolves in the melt, revealing a new surface. For the sample treated in the KCl melt, the large (110) terraces remain, but are no longer flat. The originally flat terraces are now replaced by many fine rectangular facets approximately 200 nm long and 20 nm wide. Unlike the SrCl<sub>2</sub> treatment, there is no measurable change of mass during the molten KCl treatment. The photochemical reactivities of the molten salt treated surfaces were studied with marker reactions. After the SrCl<sub>2</sub> treatment, the reactivities of both photoreduction of Ag<sup>+</sup> and photooxidation of Mn<sup>2+</sup> were enhanced, as shown in

**Fig. 3(b)** and (c). Under the same illumination conditions, small Ag or MnO<sub>2</sub> particles uniformly deposit all over the surface. Larger and more widely separated particles are also found. However, the reactivity seems to be isotropic, and no spatial selectivity was resolved. After the molten KCl treatment, shown in **Fig. 3(e)** and (f), the cathodic reactivity (Ag<sup>+</sup> reduction) seems to increase slightly, but the anodic reactivity (Mn<sup>2+</sup> oxidation) remains low.

A parallel experiment was carried out on (100) oriented SrTiO<sub>3</sub> single crystals. Topographic AFM images of a SrTiO<sub>3</sub> (100) single crystal surface that has been annealed in air at 1100 °C for 6 h is shown in **Fig. 4** (a). The annealing leads to the formation of (100) terraces and steps mostly oriented in the (100) direction. The (100) surface was reported

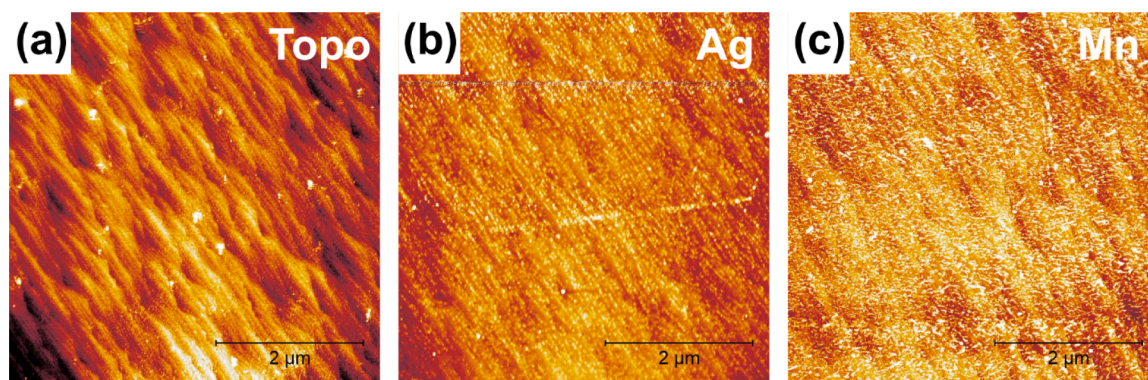


**Fig. 4.** Topographic AFM image of an air annealed SrTiO<sub>3</sub> (100) surface are given in (a). Images of the surface after photoreduction of Ag<sup>+</sup> and photooxidation of Mn<sup>2+</sup> are shown in (b) and (c). The dark-to-light vertical contrast is (a): 0–2.5 nm, (b): 0–5 nm, (c): 0–5 nm.

to be bifunctional [19], and here we found that the surface is highly reactive for both the photoreduction of Ag<sup>+</sup> and the photo-oxidation of Mn<sup>2+</sup>, as shown in Fig. 4 (b) and (c). It is found that metallic Ag deposits prefer to accumulate near the step edges while MnO<sub>2</sub> deposits nucleated all over the terrace. It is noted that the (100) surface can be terminated by a TiO<sub>2</sub> or SrO plane [27], and Paradinas et al. measured a potential difference of the two terminations to be 45 ± 10 mV [28]. A more recent study by Sharma et al. found that the water splitting reaction can proceed on (100) surfaces only when the two terminations coexist, and the SrO terminated surface provides the reaction sites and TiO<sub>2</sub> surface affects the electronic band alignment [29]. This might explain the spatial distribution of the photochemical products observed in our experiment.

The molten SrCl<sub>2</sub> and KCl treatments were carried out on the air annealed SrTiO<sub>3</sub> (100) single crystals, and the resulting surfaces were imaged by AFM and are shown in Fig. 5 (a) and (d). Like the results on

the (110) surface, both treatments changed the surface structure. After the sample was treated in the SrCl<sub>2</sub> melt, as shown in Fig. 5(a), the original terraces merged and formed new terraces as wide as 100 nm with long wavy edges, and this is a sign of Sr-rich termination [30]. As for the sample that was treated in the KCl melt, the surface is comprised of densely distributed narrow terraces that are comparable to the original ones. However, the surface also features new long, straight steps that intersect it. Again, the crystal slightly dissolved in the SrCl<sub>2</sub> melt in which the mass was reduced from 0.0635 g to 0.0602 g (~5.2 % loss), but the crystal mass remains unchanged after the KCl treatment. Photochemical properties of the two samples were explored via marker reactions. It is found that, after the molten SrCl<sub>2</sub> treatment, see Fig. 5(b) and (c), the photoanodic reactivity is almost shut off, and the photocathodic reactivity is also reduced significantly. Furthermore, the spatial distribution of the reaction products disappears as Ag particles

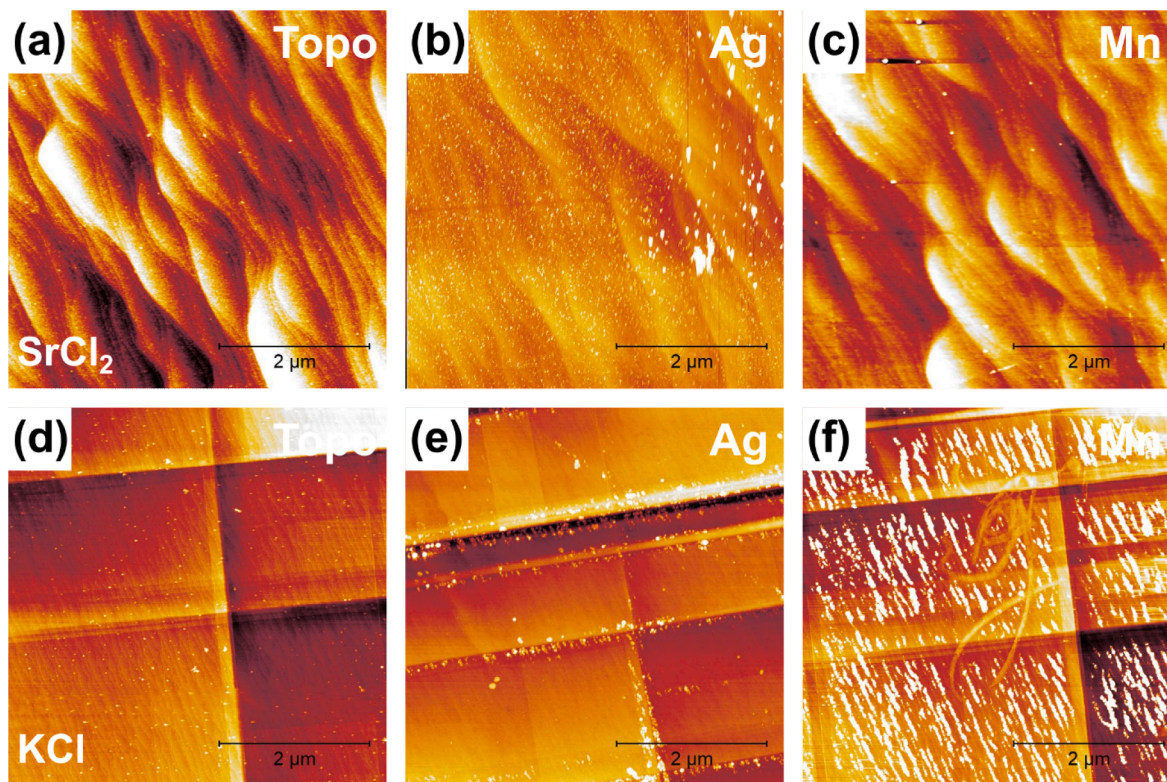


**Fig. 5.** Topographic AFM images of air annealed SrTiO<sub>3</sub> (100) single crystal surfaces after the (a) SrCl<sub>2</sub> and (d) KCl molten salt treatments. Panel (b) and (c) show AFM images of the SrCl<sub>2</sub> treated (100) surface after Ag<sup>+</sup> photoreduction and Mn<sup>2+</sup> photo-oxidation. Panel (e) and (f) show AFM images of the KCl treated (100) surface after Ag<sup>+</sup> photoreduction and Mn<sup>2+</sup> photo-oxidation. The dark-to-light vertical contrast is (a): 0–2.5 nm, (b): 0–7 nm, (c): 0–5 nm, (d): 0–7 nm, (e): 0–15 nm, (f): 0–7 nm.

uniformly deposit over the surface. As for the molten KCl treated sample, Ag deposits only accumulate near the newly formed long edges (see Fig. 5(e)), and MnO<sub>2</sub> only nucleates along certain narrow terraces (see Fig. 5(f)). The origin of this unique spatial selectivity is still under investigation.

To further understand the effect of the molten salt treatments on the surface chemistry, the surface potentials of the six samples were measured with Kelvin probe force microscope (KFM). KFM surface potential images are presented in Figure S3 and S4 for (110) surfaces and (100) surfaces, respectively. It is noted that the KFM images were recorded on the same crystals but on different locations from those in Fig. 2 to Fig. 5. The average potentials of the six crystals were determined and are shown in Table 1, along with their measured reactivities. It is found that both molten salt treatments tend to decrease the surface potential, and the SrCl<sub>2</sub> treatment has a stronger effect that renders the surface more negative. This finding is consistent on both (110) and (100) crystals.

XPS spectra were recorded on the surfaces of the six samples to study the surface compositions and chemical states. The XPS binding energy was adjusted and calibrated using the C 1s spectra at 284.7 eV as a reference (see Figure S6). It should be noted that a peak shift in binding energy of up to 1.6 eV was observed between samples annealed in air and samples treated with molten salts. This shift is attributed to alterations in the surface's electrical conductivity. Fig. 6 shows the high-resolution O 1s spectra. The O 1s spectrum can be deconvoluted into two peaks, a primary peak attributed to Ti-O bonding at 529.3 eV and a second peak attributed to surface hydroxyl groups (-OH) at 531.4 eV [31,32], shown in Fig. 6 (a) and (d). The percentage of the oxygen bonded in an -OH state is determined to be 24.9 % and 28.3 % for (100) and (110) air annealed crystals, respectively. It is found that the surface hydroxyl group density increases after both molten salt treatments. After the molten SrCl<sub>2</sub> treatment, shown in Fig. 6(b) and (e), the hydroxyl group density increases to 39.3 % and 52.3 % for (100) and (110) oriented crystals. After the KCl treatment, shown in Fig. 6(c) and (f), the hydroxyl group density increases slightly to 29.6 % and 36.2 % for (100) and (110) oriented crystals.

High resolution Sr 3d and Ti 2p XPS spectra are given in Figure S7 and Figure S8. The Sr spectrum is composed of two doublets located at 132.7 eV and 134.4 eV, corresponding to 3d<sub>5/2</sub> and 3d<sub>3/2</sub>. The doublets in the Ti spectrum located near 458.2 eV and 464.1 eV can be assigned to 2p<sub>3/2</sub> and 2p<sub>1/2</sub> of Ti<sup>4+</sup>. Note that, distinct from powdered SrTiO<sub>3</sub> samples [11,33], there is a negligible amount of Ti<sup>3+</sup> species in our single crystal samples, implying they are more stoichiometric. The Sr/Ti atomic ratios were determined from the ratio of the integrated intensities of the Sr 3d and Ti 2p spectra. The ratio is determined to be 0.88 and 0.86 for air annealed (100) and (110) single crystals, respectively, implying surfaces that are Ti-rich (Sr-depleted) compared the stoichiometry of the bulk. This might be because the vapor pressure of SrO is significantly higher than TiO<sub>2</sub> at the annealing temperature [34,35], allowing some SrO to escape during annealing. The measured ratio might also be a result of the termination. In the [100] direction, bulk SrTiO<sub>3</sub> can be terminated in to SrO and TiO<sub>2</sub> planes; while along the [110] direction, it is composed of alternating layers of SrTiO<sub>4</sub><sup>+</sup> and O<sub>2</sub><sup>4-</sup>. The results here indicate that the two molten salt treatments change the surface composition in an opposite way. The Sr/Ti ratio is measured to be 0.88 and 0.93 for the SrCl<sub>2</sub> treated (100) and (110) single crystal surfaces, respectively, suggesting that the molten salt stabilizes SrO on the (100) surface and SrTiO<sub>4</sub><sup>+</sup> on the (110) surface. However, the KCl treatment reduces the surface Sr concentration; the Sr/Ti ratio is reduced to 0.70 and 0.74 for (100) and (110) surfaces, respectively. A summary of the XPS data of the three samples is given in Table 2.

**Table 2**  
Sr/Ti ratios and surface hydroxyl groups concentrations of the six samples determined with the XPS spectra.

Treatments	Sr/Ti		-OH%	
	(100)	(110)	(100)	(110)
Air annealed	0.88	0.86	24.9 %	28.3 %
SrCl <sub>2</sub> treated	0.88	0.93	39.3 %	52.3 %
KCl treated	0.70	0.74	29.6 %	36.2 %

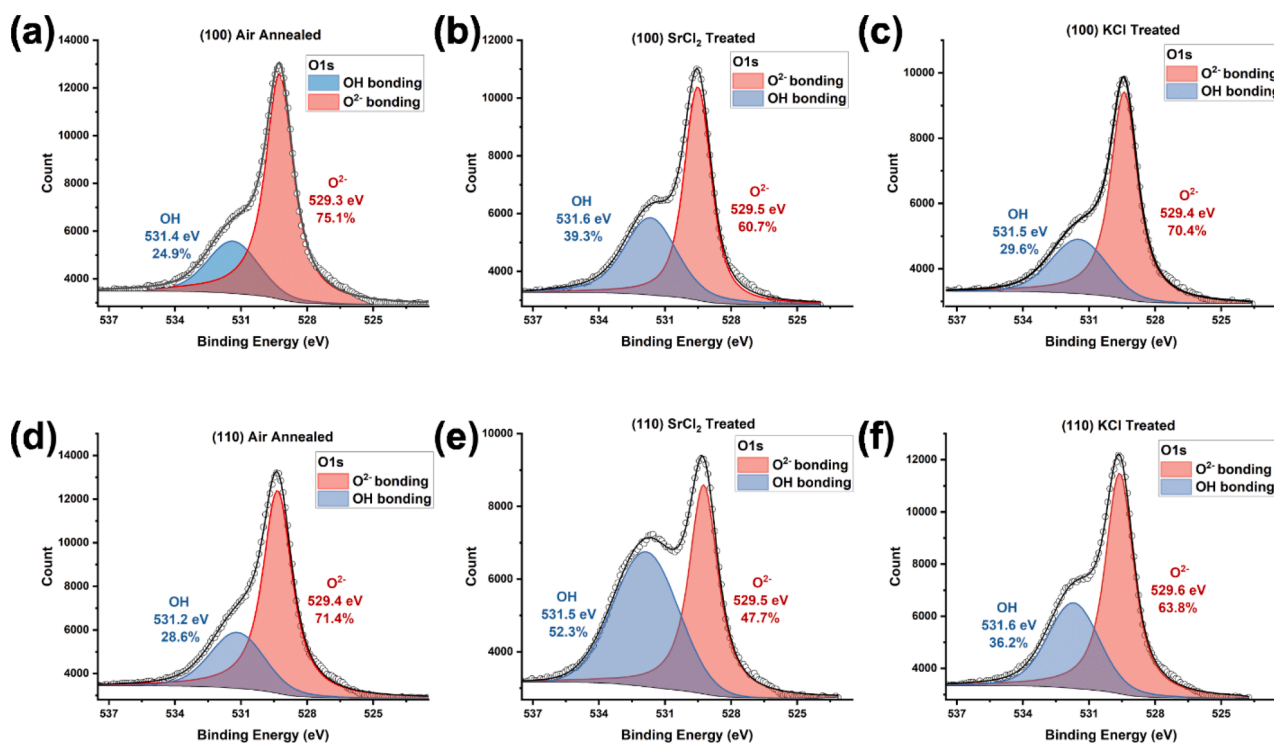


**Fig. 6.** High resolution O 1s XPS spectra of (a,b,c) (100) and (d,e,f) (110) single crystal surfaces that were (a,d) air annealed, (b,e) molten SrCl<sub>2</sub> treated, and (c,f) molten KCl treated. The peaks for oxygen atoms bonded in Ti-O and -OH are filled in red and blue, respectively.

that we have also tried to measure Al, K and Cl but cannot detect their signals via XPS, indicating the concentrations of these elements on the surface are less than the detection limit.

#### 4. Discussion

The results here clearly illustrate that the molten  $\text{SrCl}_2$  treatment has a significant influence on the structure and chemical composition of  $\text{SrTiO}_3$  surface. The first apparent difference between  $\text{SrCl}_2$  and KCl is that the  $\text{SrTiO}_3$  surface slightly dissolves in the molten  $\text{SrCl}_2$  with a consistent 3–5 % mass loss. There is no detectable loss of mass in the KCl melt. Yamakata et al. proposed that  $\text{SrTiO}_3$  dissolves and recrystallizes in the  $\text{SrCl}_2$  melt, so that the crystal morphology changes, and the crystallinity is improved [5]. However, considering that particle shape and size is not significantly changed during the treatment, as shown in Fig. 1(a), it is not feasible that the particle completely dissolves and recrystallizes. Based on the results here, a small amount of material dissolves in the melt. Different from what happens in the single crystal experiment, the material that dissolves from the powder might diffuse between particles, promoting coarsening [36] or Ostwald ripening [37]. If so, some of the smaller particles would disappear and the average particle size would increase [5,6]. However, based on micrographs such as the images in Fig. 1, coarsening is not significant, if it occurs at all.

The XPS spectra indicate that the molten salt treatment increases the concentration of hydroxyls on the surface, and the KFM studies suggest that the treatment decreases the surface potential. For both of these trends, the influence of molten  $\text{SrCl}_2$  is greater than molten KCl. The hydroxyl concentrations have been correlated to the surface potentials of the six samples, plotted in Fig. 7(a), indicating that hydroxyl groups induce a negative (anodic) surface, which is consistent with the results by Zhu et al. [32]. Past studies agree that surface hydroxyl groups are good hole traps, promoting the anodic reaction and elongating the charge carrier lifetime [38,39]. Secondly, surface hydroxyl groups are determined to be one of the primary water adsorption sites since the protonated lattice of oxides easily form hydrogen bonds with water molecules [29,40]. In our case, we only load reduction cocatalysts so that the anodic reaction is supposed to occur on the  $\text{SrTiO}_3$  surface. Since

the overall reaction rate depends on the slower one of the two half-reactions [21], the promotion of the photoanodic reaction driven by the hydroxyl-rich surface will improve the overall reaction rate. It is also concluded that this effect is orientation dependent; from the KFM data in Fig. 7(b), the potential of the (110) surface is reduced much more than the potential of the (100) surface. This will increase the potential difference between the two oriented surfaces from 0.07 V to 0.21 V, a situation that enhances the charge separation inside the particle. The charge separation between the (100) and (110) surfaces in  $\text{SrTiO}_3$  has been extensively investigated [9,22,41–43]. Su et al. measured the surface charge on (100) and (110) facets of undoped  $\text{SrTiO}_3$  particles in an aqueous electrolyte, and the potential difference between the two surfaces was measured to be 40 mV [44], a little lower than our measurement (71 mV for the air annealed sample). This is reasonable since we measured the potential in air, and solution species might adsorb to the surface and compensate the charge.

We assume that the increase in the measured potential differences between the single crystal (100) and (110) surfaces treated in  $\text{SrCl}_2$  also occurs on a  $\text{SrCl}_2$  treated  $\text{SrTiO}_3$  particles, and this is beneficial to photocatalytic reactivity. The anisotropic surface potential within a particulate photocatalyst could induce different degrees of band bending for the two surfaces. The (100) surface with a more positive potential has reduced upward band bending at the surface, therefore, it is easier for photogenerated electrons to reach the surface and participate in photocathodic reactions. Conversely, the (110) surface, with a more negative potential and increased upward band bending, attracts more photogenerated holes towards its surface. Thus, it promotes photoanodic reactions [32]. The potential difference between the (100) and (110) surfaces results in an internal electric field that facilitates the migration of photogenerated charge carriers. Here, holes migrate toward the more negative (110) surface. An increase in potential difference between the (100) and (110) surfaces can lead to a stronger electric field, which in turn can enhance the extent of anisotropic charge separation [10]. This phenomenon has been observed not only in the {100} and {110} surfaces of  $\text{SrTiO}_3$  photocatalysts, but also in the {001} and {111} surfaces of  $\text{Cu}_2\text{O}$  [45], {010} and {110} surfaces of  $\text{BiVO}_4$  [46], and {001} and {200} surfaces of  $\text{BiOBr}$  [47]. In the case of

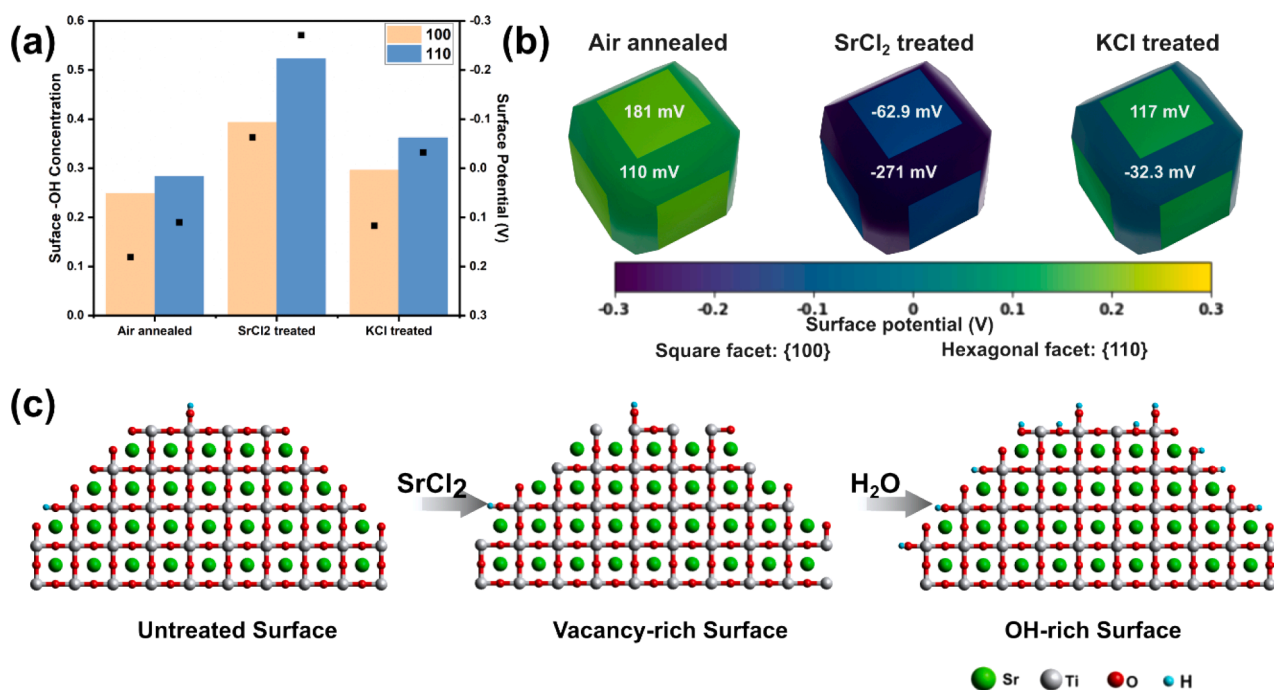


Fig. 7. (a) Surface hydroxyl group concentrations (shown as bars) and surface potential (shown as dots) of the six samples. (b) Schematic illustration of the change of surface potential induced by the molten  $\text{SrCl}_2$  and KCl treatments. (c) Schematic illustration of the possible mechanism of the hydroxyl group-rich surface.

the molten SrCl<sub>2</sub> treatment (as shown in Fig. 7(b)), an increase in the potential difference from 71 mV to 208 mV can contribute to charge separation and enhance the photocatalytic reactivity.

It is interesting to speculate about how the molten SrCl<sub>2</sub> treatment produces a surface with a high density of hydroxyl groups. When water adsorbs and dissociates on SrTiO<sub>3</sub> surface, a hydroxyl group can bond to a strontium site (Sr-OH), a titanium site (Ti-OH), or directly on an oxygen site (O-H) [40]. It has been reported that Sr-rich surfaces are more easily hydroxylated compared with Ti-rich surfaces [48,49], so that increasing Sr/Ti atomic ratio on the surface might contribute to the increased hydroxyl concentration. However, based on the XPS data in Table 2, the changes of surface hydroxyl concentration and Sr/Ti are not proportional, implying another factor influences the system. One possibility is that added hydroxyl groups occupy vacant O sites created during the SrCl<sub>2</sub> treatment. Based on the phase diagram, it is known that under these conditions SrO will form in the melt and one source of oxygen is the SrTiO<sub>3</sub>, which we know to be partially dissolving. If numerous oxygen vacancies are created on the surface, with their charge compensated by metal vacancies, hydroxyl groups can directly fill these vacancies during rinsing in water. In this case, a water molecule dissociates into an OH group that fills the vacancy, and a H atom binds to another bridging O site, forming a pair of hydroxyl groups [50,51]. This effect has also been observed on BaTiO<sub>3</sub> surfaces [52]. It is also possible that surface oxygen atoms are initially replaced by Cl<sup>-</sup> in the melt, and then replaced by hydroxyl groups during washing, leading to the same result. However, if this happened in SrCl<sub>2</sub>, it would probably also happen equally in the KCl melt, so the first proposal seems more likely. A schematic of the proposed hydroxyl substitution process is shown in Fig. 7(c).

## 5. Conclusion

The influence of the molten SrCl<sub>2</sub> treatment on the surface of SrTiO<sub>3</sub> has been studied in comparison to substrates annealed in air and substrates annealed in molten KCl. In the KCl melt, the surfaces of SrTiO<sub>3</sub> crystals reconstruct, changing the spatial distribution of photocathodic and photoanodic reaction sites. When SrTiO<sub>3</sub> is treated in molten SrCl<sub>2</sub> in Al<sub>2</sub>O<sub>3</sub> crucibles, a small amount of the SrTiO<sub>3</sub> dissolves in the melt, reducing the mass of the crystal by 3–5%. Furthermore, the molten salt undergoes a reaction with the alumina crucible, resulting in the formation of Sr<sub>3</sub>Al<sub>2</sub>O<sub>6</sub>. This reaction continues until the salt is consumed, before the end of the thermal treatment. KFM studies indicate that the treatment reduces the surface potential, and the potential drop depends on crystallographic orientation. As a result, the potential difference between (100) and (110) surfaces increases from 0.07 V to 0.21 V, building a much stronger electric field inside the particle and promoting charge separation. The measured decrease of surface potential is proportional to the increase of the surface hydroxyl group concentration. Because hydroxyl groups serve as hole traps and promote the rate limiting photoanodic half reaction, the overall reactivity is improved.

## CRedit authorship contribution statement

**Mingyi Zhang:** Investigation, Data curation, Formal analysis, Writing – original draft. **Zhitao Guo:** Investigation, Data curation, Formal analysis. **Andrew J. Gellman:** Conceptualization, Methodology, Supervision, Writing – review & editing. **Paul A. Salvador:** Conceptualization, Supervision, Writing – review & editing. **Gregory S. Rohrer:** Conceptualization, Supervision, Funding acquisition, Project administration, Resources, Writing – review & editing.

## Declaration of Competing Interest

The authors declare that they have no known competing financial interests or personal relationships that could have appeared to influence the work reported in this paper.

## Data availability

Data will be made available on request.

## Acknowledgements

This work was supported by the National Science Foundation under Grant Number: DMR 2016267, and the authors acknowledge the use of the Materials Characterization Facility at Carnegie Mellon University supported by Grant Number: MCF-677785.

## Appendix A. Supplementary material

Supplementary data to this article can be found online at <https://doi.org/10.1016/j.apsusc.2023.158111>.

## References

- [1] Q. Wang, K. Domen, Particulate Photocatalysts for Light-Driven Water Splitting: Mechanisms, Challenges, and Design Strategies, *Chem. Rev.* 120 (2020) 919–985, <https://doi.org/10.1021/acs.chemrev.9b00201>.
- [2] X. Tao, Y. Zhao, S. Wang, C. Li, R. Li, Recent advances and perspectives for solar-driven water splitting using particulate photocatalysts, *Chem. Soc. Rev.* 51 (2022) 3561–3608, <https://doi.org/10.1039/D1CS01182K>.
- [3] Z. Wang, C. Li, K. Domen, Recent developments in heterogeneous photocatalysts for solar-driven overall water splitting, *Chem. Soc. Rev.* 48 (2019) 2109–2125, <https://doi.org/10.1039/C8CS00542G>.
- [4] H. Kato, M. Kobayashi, M. Hara, M. Kakihana, Fabrication of SrTiO<sub>3</sub> exposing characteristic facets using molten salt flux and improvement of photocatalytic activity for water splitting, *Catal. Sci. Technol.* 3 (2013) 1733–1738, <https://doi.org/10.1039/C3CY00014A>.
- [5] A. Yamakata, H. Yeilin, M. Kawaguchi, T. Hisatomi, J. Kubota, Y. Sakata, K. Domen, Morphology-sensitive trapping states of photogenerated charge carriers on SrTiO<sub>3</sub> particles studied by time-resolved visible to Mid-IR absorption spectroscopy: The effects of molten salt flux treatments, *J. Photochem. Photobiol. Chem.* 313 (2015) 168–175, <https://doi.org/10.1016/j.jphotochem.2015.05.016>.
- [6] Y. Ham, T. Hisatomi, Y. Goto, Y. Moriya, Y. Sakata, A. Yamakata, J. Kubota, K. Domen, Flux-mediated doping of SrTiO<sub>3</sub> photocatalysts for efficient overall water splitting, *J. Mater. Chem. A* 4 (2016) 3027–3033, <https://doi.org/10.1039/C5TA04843E>.
- [7] T.H. Chiang, H. Lyu, T. Hisatomi, Y. Goto, T. Takata, M. Katayama, T. Minegishi, K. Domen, Efficient Photocatalytic Water Splitting Using Al-Doped SrTiO<sub>3</sub> Coloaded with Molybdenum Oxide and Rhodium-Chromium Oxide, *ACS Catal.* 8 (2018) 2782–2788, <https://doi.org/10.1021/acscatal.7b04264>.
- [8] H. Lyu, T. Hisatomi, Y. Goto, M. Yoshida, T. Higashi, M. Katayama, T. Takata, T. Minegishi, H. Nishiyama, T. Yamada, Y. Sakata, K. Asakura, K. Domen, An Al-doped SrTiO<sub>3</sub> photocatalyst maintaining sunlight-driven overall water splitting activity for over 1000 h of constant illumination, *Chem. Sci.* 10 (2019) 3196–3201, <https://doi.org/10.1039/C8SC05757E>.
- [9] M. Zhang, P.A. Salvador, G.S. Rohrer, Influence of particle size and shape on the rate of hydrogen produced by Al-doped SrTiO<sub>3</sub> photocatalysts, *J. Am. Ceram. Soc.* 105 (2022) 5336–5346, <https://doi.org/10.1111/jace.18488>.
- [10] T. Takata, J. Jiang, Y. Sakata, M. Nakabayashi, N. Shibata, V. Nandal, K. Seki, T. Hisatomi, K. Domen, Photocatalytic water splitting with a quantum efficiency of almost unity, *Nature* 581 (2020) 411–414, <https://doi.org/10.1038/s41586-020-2278-9>.
- [11] Z. Zhao, R.V. Goncalves, S.K. Barman, E.J. Willard, E. Byle, R. Perry, Z. Wu, M. N. Huda, A.J. Moulé, F.E. Osterloh, Electronic structure basis for enhanced overall water splitting photocatalysis with aluminum doped SrTiO<sub>3</sub> in natural sunlight, *Energy Env. Sci.* 12 (2019) 1385–1395, <https://doi.org/10.1039/C9EE00310J>.
- [12] Y. Qin, F. Fang, Z. Xie, H. Lin, K. Zhang, X. Yu, K. Chang, La, Al-Codoped SrTiO<sub>3</sub> as a Photocatalyst in Overall Water Splitting: Significant Surface Engineering Effects on Defect Engineering, *ACS Catal.* 11 (2021) 11429–11439, <https://doi.org/10.1021/acscatal.1c02874>.
- [13] J. Cui, X. Yang, Z. Yang, Y. Sun, X. Chen, X. Liu, D. Wang, S. Jiang, L. Liu, J. Ye, Zr–Al co-doped SrTiO<sub>3</sub> with suppressed charge recombination for efficient photocatalytic overall water splitting, *Chem. Commun.* 57 (2021) 10640–10643, <https://doi.org/10.1039/D1CC04514H>.
- [14] Z. Su, W. Chen, N. Wang, Y. Wan, Z. Huang, S. Liu, D. Guo, F. Fang, K. Chang, Designing Slight Ta<sup>5+</sup> to Balance Al<sup>3+</sup> for Enhanced Defect Engineering in SrTiO<sub>3</sub> for Overall Water Splitting, *Catal. Lett.* (2022), <https://doi.org/10.1007/s10562-022-04179-w>.
- [15] Z. Zhao, E.J. Willard, H. Li, Z. Wu, R.H.R. Castro, F.E. Osterloh, Aluminum enhances photochemical charge separation in strontium titanate nanocrystal photocatalysts for overall water splitting, *J. Mater. Chem. A* 6 (2018) 16170–16176, <https://doi.org/10.1039/C8TA05885G>.
- [16] L. Dong, H. Shi, K. Cheng, Q. Wang, W. Weng, W. Han, Shape-controlled growth of SrTiO<sub>3</sub> polyhedral submicro/nanocrystals, *Nano Res.* 7 (2014) 1311–1318, <https://doi.org/10.1007/s12274-014-0495-y>.
- [17] K. Maeda, K. Teramura, H. Masuda, T. Takata, N. Saito, Y. Inoue, K. Domen, Efficient Overall Water Splitting under Visible-Light Irradiation on (Ga<sub>1-x</sub>Zn<sub>x</sub>)(N<sub>1-x</sub>

- $\text{O}_x$ ) Dispersed with Rh–Cr Mixed-Oxide Nanoparticles: Effect of Reaction Conditions on Photocatalytic Activity, *J. Phys. Chem. B* 110 (2006) 13107–13112, <https://doi.org/10.1021/jp0616563>.
- [18] J.L. Giocondi, G.S. Rohrer, Spatially Selective Photochemical Reduction of Silver on the Surface of Ferroelectric Barium Titanate, *Chem. Mater.* 13 (2001) 241–242, <https://doi.org/10.1021/cm000890h>.
- [19] J.L. Giocondi, G.S. Rohrer, Structure sensitivity of photochemical oxidation and reduction reactions on SrTiO<sub>3</sub> surfaces, *J. Am. Ceram. Soc.* 86 (2003) 1182–1189, <https://doi.org/10.1111/j.1151-2916.2003.tb03445.x>.
- [20] A.S. Pisat, G.S. Rohrer, P.A. Salvador, Spatial selectivity of photodeposition reactions on polar surfaces of centrosymmetric ferroelastic gamma-WO<sub>3</sub>, *J. Mater. Chem. A* 5 (2017) 8261–8266, <https://doi.org/10.1039/c7ta00842b>.
- [21] N. Zhang, P.A. Salvador, G.S. Rohrer, Influence of pH and Surface Orientation on the Photochemical Reactivity of SrTiO<sub>3</sub>, *ACS Appl. Mater. Interfaces* (2020), <https://doi.org/10.1021/acscami.0c04351>.
- [22] A.S. Pisat, P.A. Salvador, G.S. Rohrer, The Facet Structure and Photochemical Reactivity of Arbitrarily Oriented Strontium Titanate Surfaces, *Adv. Mater. Interfaces* 6 (2019) 1900731, <https://doi.org/10.1002/admi.201900731>.
- [23] N. David, K. Petr, Gwyddion: an open-source software for SPM data analysis, *Open Phys.* 10 (2012) 181, <https://doi.org/10.2478/s11534-011-0096-2>.
- [24] E.M. Lopato, E.A. Eikey, Z.C. Simon, S. Back, K. Tran, J. Lewis, J.F. Kowalewski, S. Yazdi, J.R. Kitchin, Z.W. Ulissi, J.E. Millstone, S. Bernhard, Parallelized Screening of Characterized and DFT-Modeled Bimetallic Colloidal Cocatalysts for Photocatalytic Hydrogen Evolution, *ACS Catal.* 10 (2020) 4244–4252, <https://doi.org/10.1021/acscatal.9b05404>.
- [25] T. Kimura, Molten salt synthesis of ceramic powders, *Adv. Ceram.-Synth. Charact. Process. Specif. Appl.* (2011) 75–100.
- [26] B. Neumann, C. Kröger, H. Jüttner, Die Systeme Erdalkalichlorid-Erdalkalioxyd und die Zersetzung der Erdalkalichloride durch Wasserdampf, *Z. Für Elektrochem. Angew. Phys. Chem.* 41 (1935) 725–736, <https://doi.org/10.1002/bbpc.19350411005>.
- [27] G. Koster, B.L. Kropman, G.J.H.M. Rijnders, D.H.A. Blank, H. Rogalla, Quasi-ideal strontium titanate crystal surfaces through formation of strontium hydroxide, *Appl. Phys. Lett.* 73 (1998) 2920–2922, [10.1063/1.122630](https://doi.org/10.1063/1.122630).
- [28] M. Paradinas, L. Garzón, F. Sánchez, R. Bachelet, D.B. Amabilino, J. Fontcuberta, C. Ocal, Tuning the local frictional and electrostatic responses of nanostructured SrTiO<sub>3</sub>—surfaces by self-assembled molecular monolayers, *Phys. Chem. Chem. Phys.* 12 (2010) 4452–4458, <https://doi.org/10.1039/B924227A>.
- [29] V. Sharma, B. Bein, A. Lai, B. Pamuk, C.E. Dreyer, M. Fernández-Serra, M. Dawber, Cooperative Interactions between Surface Terminations Explain Photocatalytic Water Splitting Activity on SrTiO<sub>3</sub>, *PRX Energy.* 1 (2022) 23002, <https://doi.org/10.1103/PRXEnergy.1.023002>.
- [30] C. Baumer, C. Xu, F. Gunkel, N. Raab, R.A. Heinen, A. Koehl, R. Dittmann, Surface Termination Conversion during SrTiO<sub>3</sub> Thin Film Growth Revealed by X-ray Photoelectron Spectroscopy, *Sci. Rep.* 5 (2015) 11829, <https://doi.org/10.1038/srep11829>.
- [31] G. Vovk, X. Chen, C.A. Mims, In Situ XPS Studies of Perovskite Oxide Surfaces under Electrochemical Polarization, *J. Phys. Chem. B* 109 (2005) 2445–2454, <https://doi.org/10.1021/jp0486494>.
- [32] Y. Zhu, P.A. Salvador, G.S. Rohrer, Controlling the Relative Areas of Photocathodic and Photoanodic Terraces on the SrTiO<sub>3</sub>(111) Surface, *Chem. Mater.* 28 (2016) 5155–5162, <https://doi.org/10.1021/acs.chemmater.6b02205>.
- [33] Z. Su, F. Fang, X. Li, W. Han, X. Liu, K. Chang, Synergistic surface oxygen defect and bulk Ti<sup>3+</sup> defect engineering on SrTiO<sub>3</sub> for enhancing photocatalytic overall water splitting, *J. Colloid Interface Sci.* 626 (2022) 662–673, <https://doi.org/10.1016/j.jcis.2022.06.109>.
- [34] R.H. Lamoreaux, D.L. Hildenbrand, L. Brewer, High-Temperature Vaporization Behavior of Oxides II. Oxides of Be, Mg, Ca, Sr, Ba, B, Al, Ga, In, Tl, Si, Ge, Sn, Pb, Zn, Cd, and Hg, *J. Phys. Chem. Ref. Data.* 16 (1987) 419–443, [10.1063/1.555799](https://doi.org/10.1063/1.555799).
- [35] Z. Wang, F. Yang, Z. Zhang, Y. Tang, J. Feng, K. Wu, Q. Guo, J. Guo, Evolution of the surface structures on SrTiO<sub>3</sub>(110) tuned by Ti or Sr concentration, *Phys. Rev. B* 83 (2011), 155453, <https://doi.org/10.1103/PhysRevB.83.155453>.
- [36] R.V. Day, J. Barford, Particle Coarsening in the Solid State, *Nature* 217 (1968) 1145–1146, <https://doi.org/10.1038/2171145a0>.
- [37] P.W. Voorhees, The theory of Ostwald ripening, *J. Stat. Phys.* 38 (1985) 231–252, <https://doi.org/10.1007/BF01017860>.
- [38] K. Shirai, G. Fazio, T. Sugimoto, D. Selli, L. Ferraro, K. Watanabe, M. Haruta, B. Ohtani, H. Kurata, C. Di Valentin, Y. Matsumoto, Water-Assisted Hole Trapping at the Highly Curved Surface of Nano-TiO<sub>2</sub> Photocatalyst, *J. Am. Chem. Soc.* 140 (2018) 1415–1422, <https://doi.org/10.1021/jacs.7b11061>.
- [39] D. Lawless, N. Serpone, D. Meisel, Role of hydroxyl radicals and trapped holes in photocatalysis. A pulse radiolysis study, *J. Phys. Chem.* 95 (1991) 5166–5170, <https://doi.org/10.1021/j100166a047>.
- [40] N. Domingo, E. Pach, K. Cordero-Edwards, V. Pérez-Dieste, C. Escudero, A. Verdaguer, Water adsorption, dissociation and oxidation on SrTiO<sub>3</sub> and ferroelectric surfaces revealed by ambient pressure X-ray photoelectron spectroscopy, *Phys. Chem. Chem. Phys.* 21 (2019) 4920–4930, <https://doi.org/10.1039/C8CP07632D>.
- [41] L. Mu, Y. Zhao, A. Li, S. Wang, Z. Wang, J. Yang, Y. Wang, T. Liu, R. Chen, J. Zhu, F. Fan, R. Li, C. Li, Enhancing charge separation on high symmetry SrTiO<sub>3</sub> exposed with anisotropic facets for photocatalytic water splitting, *Energ. Environ. Sci.* 9 (2016) 2463–2469, <https://doi.org/10.1039/c6ee00526h>.
- [42] P.-L. Hsieh, G. Naresh, Y.-S. Huang, C.-W. Tsao, Y.-J. Hsu, L.-J. Chen, M.H. Huang, Shape-Tunable SrTiO<sub>3</sub> Crystals Revealing Facet-Dependent Optical and Photocatalytic Properties, *J. Phys. Chem. C* 123 (2019) 13664–13671, <https://doi.org/10.1021/acs.jpcc.9b02081>.
- [43] Q. Jia, C. Wang, J. Liu, X. Cai, L. Zhong, S. Chen, T. Li, G. Yu, L. Wu, D. Duan, Synergistic Effect of Sr-O Divacancy and Exposing Facets in SrTiO<sub>3</sub> Micro/Nano Particle: Accelerating Exciton Formation and Splitting, Highly Efficient Co<sup>2+</sup> Photooxidation, *Small* 18 (2022) 2202659, <https://doi.org/10.1002/sml.202202659>.
- [44] S. Su, I. Siretanu, D. van den Ende, B. Mei, G. Mul, F. Mugele, Facet-Dependent Surface Charge and Hydration of Semiconducting Nanoparticles at Variable pH, *Adv. Mater.* 33 (2021) 2106229, <https://doi.org/10.1002/adma.202106229>.
- [45] R. Chen, Z. Ren, Y. Liang, G. Zhang, T. Dittrich, R. Liu, Y. Liu, Y. Zhao, S. Pang, H. An, C. Ni, P. Zhou, K. Han, F. Fan, C. Li, Spatiotemporal imaging of charge transfer in photocatalyst particles, *Nature* 610 (2022) 296–301, <https://doi.org/10.1038/s41586-022-05183-1>.
- [46] X. Mao, P. Chen, Inter-facet junction effects on particulate photoelectrodes, *Nat. Mater.* 21 (2022) 331–337, <https://doi.org/10.1038/s41563-021-01161-6>.
- [47] Z. Luo, X. Ye, S. Zhang, S. Xue, C. Yang, Y. Hou, W. Xing, R. Yu, J. Sun, Z. Yu, X. Wang, Unveiling the charge transfer dynamics steered by built-in electric fields in BiOBr photocatalysts, *Nat. Commun.* 13 (2022) 2230, <https://doi.org/10.1038/s41467-022-29825-0>.
- [48] J.D. Baniecki, M. Ishii, T. Shioga, K. Kurihara, S. Miyahara, Surface core-level shifts of strontium observed in photoemission of barium strontium titanate thin films, *Appl. Phys. Lett.* 89 (2006), <https://doi.org/10.1063/1.2357880>.
- [49] H. Guhl, W. Müller, K. Reuter, Water adsorption and dissociation on SrTiO<sub>3</sub>(001) revisited: A density functional theory study, *Phys. Rev. B* 81 (2010), 155455, <https://doi.org/10.1103/PhysRevB.81.155455>.
- [50] G. Ketteler, S. Yamamoto, H. Blumh, K. Andersson, D.E. Starr, D.F. Ogletree, H. Ogasawara, A. Nilsson, M. Salmeron, The Nature of Water Nucleation Sites on TiO<sub>2</sub>(110) Surfaces Revealed by Ambient Pressure X-ray Photoelectron Spectroscopy, *J. Phys. Chem. C* 111 (2007) 8278–8282, <https://doi.org/10.1021/jp068606i>.
- [51] W. Li, S. Liu, S. Wang, Q. Guo, J. Guo, The Roles of Reduced Ti Cations and Oxygen Vacancies in Water Adsorption and Dissociation on SrTiO<sub>3</sub>(110), *J. Phys. Chem. C* 118 (2014) 2469–2474, <https://doi.org/10.1021/jp409076y>.
- [52] J.L. Wang, F. Gaillard, A. Pancotti, B. Gautier, G. Niu, B. Vilquin, V. Pillard, G.L.M. P. Rodrigues, N. Barrett, Chemistry and Atomic Distortion at the Surface of an Epitaxial BaTiO<sub>3</sub> Thin Film after Dissociative Adsorption of Water, *J. Phys. Chem. C* 116 (2012) 21802–21809, <https://doi.org/10.1021/jp305826e>.